Laser & Photonics Reviews

LASER & PHOTONICS REVIEWS

www.lpr-journal.org

RESEARCH ARTICLE

Inorganic K_2SiF_6: Mn^{4+} Luminescent Layers @ Cu Composites Prepared via Sintering-Free Process for Laser-Driven Projection Display

Sifan Zhuo[1] | Huaixi Chen[2] | Xiaolong Liu[3] | Shisheng Lin[1] | Lingwei Zeng[4] | Hewen Lin[1] | Yongcai Dai[1] | Ran An[1] | Dahai Hu[1] | Huaxiang Qiu[1] | Feng Huang[1] | Daqin Chen[1,5]

[1]College of Physics and Energy, Fujian Normal University, Fuzhou, Fujian, P. R. China | [2]Key Laboratory of Opto-Electronic Science and Technology for Medicine of Ministry of Education, College of Photonic and Electronic Engineering, Fujian Normal University, Fuzhou, Fujian, P. R. China | [3]Jomoo Kitchen &Bath Co., LTD, Quanzhou, Fujian, P. R. China | [4]School of Chemistry and Chemical Engineering, Key Laboratory of Theoretical Organic Chemistry and Functional Molecule of Ministry of Education, Hunan University of Science and Technology, Xiangtan, Hunan, P. R. China | [5]Fujian Provincial Engineering Technology Research Center of Solar Energy Conversion and Energy Storage, Fujian Normal University, Fuzhou, Fujian, P. R. China

Correspondence: Huaixi Chen (chenhx@fjnu.edu.cn) | Shisheng Lin (linshisheng@fjnu.edu.cn) | Daqin Chen (dqchen@fjnu.edu.cn)

Received: 26 January 2026 | **Revised:** 19 March 2026 | **Accepted:** 27 March 2026

Keywords: glass | K_2SiF_6: Mn^{4+} | laser-driven display | luminescent materials | phosphors

ABSTRACT

High-brightness narrow-band red color converters are essential for laser-driven wide-color-gamut displays, but challenges remain in their practical development. Although K_2SiF_6: Mn^{4+} (KSF: Mn^{4+}) phosphors offer ultra-narrowband emission and high color purity, their integration into bulk converters often suffers from thermal degradation, interfacial damage, and severe luminescence quenching under high-power blue laser excitation. Here, a KSF: Mn^{4+} inorganic luminescent layer is coupled with a metal substrate via a sintering-free fabrication strategy, facilitating the development of a KSF: Mn^{4+}-TiO_2/BN@Cu composite (K-TB@Cu). In this architecture, a TiO_2/h-BN transition layer is deliberately introduced to simultaneously enhance the optical reflectivity of the substrate and promote efficient heat dissipation from the KSF: Mn^{4+} phosphor to the Cu substrate. The optimized composite delivers a red output power of 399.7 mW in the static reflective mode and up to 3029 mW in the rotated reflective mode, while maintaining a low surface temperature (~52.4°C). Further, revealed from comparative evaluations in a laser-driven projection display system, among the investigated composite configurations, K-TB@Cu uniquely delivers ultra-narrowband red emission with high color purity, intense brightness, and robust operational stability. These characteristics position K-TB@Cu as a highly promising candidate for next-generation laser-driven display applications.

1 | Introduction

For wide-color-gamut displays, high-brightness narrow-band lighting sources are essential, and laser diodes (LDs) clearly outperform light-emitting diodes (LEDs) due to their superior directionality, monochromaticity, and ability to avoid efficiency drops [1–5]. However, the application of lasers for all RGB sources encounters challenges, including imaging speckle induced by laser coherence and the complexities associated with the production of high-power green lasers [6–11]. As such, laser-driven lighting source (blue laser coupled with color converters) has emerged as an effective alternative, but high-performance laser-driven narrow-band color converters remain extremely scarce [12–19].

Accordingly, all-inorganic color converters have gained significant attention, including materials such as single crystals,

transparent ceramics, glass ceramics, phosphor-in-glass (PiG), and phosphor-in-glass film (PiGF). Preparation methods can be broadly categorized into two types: luminescent bulk direct synthesis and luminescent powder embedding [20–24]. The former type involves processes such as solid-state reactions to generate luminescent bulk materials, while the latter applies pre-existing luminescent particles as raw materials, embedding them into bulk materials. For the latter method, such as PiG and PiGF, the adaptable choice of embedded phosphor and the flexibility in spectral design provide a natural advantage in achieving narrow-band emission performance [25–27]. Further, from the perspective of the luminescent system, narrow-band green-emitting color converters have initially received considerable attention, achieving a series of significant breakthroughs, such as β-SiAlON: Eu^{2+} PiGF and Al_2O_3-$LaMgAl_{11}O_{19}$: Mn^{2+} transparent composite ceramics [28, 29]. However, research on equally significant laser-driven narrow-band red-emitting materials remains relatively scarce and encounters challenges. Specifically: (1) Red-emitting $CsPb(Br, I)_3$-related materials are expected to enable high-performance displays, but their potential is constrained by laser-driven stability; (2) Traditional Eu^{2+}-doped luminescent systems struggle to achieve efficient narrow-band red light emission [30, 31]. Evidently, further research is required to fully exploit the commercially available narrow-band red-emitting K_2SiF_6: Mn^{4+} (KSF: Mn^{4+}), thereby benefiting practical applications.

However, in fluoride systems such as KSF: Mn^{4+}, when the material transitions from powder form to PiG/PiGF bulk form, the destructive effects of co-sintering, resulting from both the thermal degradation of the phosphor and the interactions between the phosphor and the amorphous glass, are often pronounced and difficult to avoid. Meanwhile, for laser-driven color converters, the photo-thermal synergy is crucial, as the simultaneous occurrence of optical saturation and thermal saturation significantly increases the non-radiative recombination rate under high-power blue laser excitation, ultimately leading to luminescence quenching. If an inorganic luminescent layer could be combined with inexpensive high-thermal-conductivity metals, it would provide a material composite approach that balances cost and performance [32–35]. Nevertheless, the mismatch in thermal expansion creates challenges in coupling the metallic substrate with the inorganic material by sintering. Building on the aforementioned considerations, the preparation of high-performance narrow-band luminescent composites via sintering-free technology is worth significant attention, which enables the nondestructive embedding of fluoride phosphors and shows great promise for coupling materials with markedly different thermal expansion coefficients [36–39].

In this study, a KSF: Mn^{4+} inorganic luminescent layer was coupled with a metal substrate via a sintering-free fabrication strategy, facilitating the development of a KSF: Mn^{4+}-TiO_2/BN@Cu composite (denoted as K-TB@Cu). In this architecture, a TiO_2/h-BN (TB) transition layer was deliberately introduced to simultaneously enhance the optical reflectivity of the substrate and promote efficient heat dissipation from the KSF: Mn^{4+} phosphor to the Cu substrate. Through systematic optimization of key parameters, including the thickness, the relative proportion of TiO_2 and h-BN in the TB layer, the K-TB@Cu composite achieved an optimized red output power of 399.7 mW under static reflective operation. Moreover, under the rotated reflective mode, K-TB@Cu exhibited a markedly superior performance compared to the static configuration, delivering a maximum red output power of 3029 mW while maintaining a low surface temperature of approximately 52.4°C. Notably, the composite retained 98.7% of its initial luminescence after 180 s of continuous irradiation with an 11 W blue laser (4.33 W mm^{-2}), exhibiting excellent thermal and photostability. Further, revealed from comparative evaluations in a laser-driven projection system, among the investigated composite configurations, K-TB@Cu uniquely delivers ultra-narrowband red emission with high color purity, intense brightness, and robust operational stability. These attributes position K-TB@Cu as a highly promising candidate for next-generation laser-driven display applications.

2 | Results and Discussion

Figure 1 schematically depicts the fabrication process of the K-TB@Cu, in which a TB interlayer was prepared by scraping a homogeneous mixture of TiO_2, h-BN, and Al_2O_3-based adhesive onto a Cu substrate (the dimensions: 1.5 × 1.5 × 0.3 mm). Subsequently, a slurry containing KSF: Mn^{4+} phosphor, formulated using an analogous procedure, was uniformly applied onto the TB layer. The resulting assembly was then cured at ambient conditions for 2 h, yielding the final composite. The particle size distributions and morphologies of TiO_2 powder, h-BN powder, and KSF: Mn^{4+} powder are illustrated in Figures S1–S3. The corresponding particle sizes are approximately 1.1–1.3 μm, 60–87 nm, and 11–15.8 μm, respectively. Meanwhile, with Al_2O_3 as its primary constituent, the used Al_2O_3 adhesive is an inorganic binder that can be cured at room temperature. The x-ray diffraction (XRD) patterns of the Al_2O_3 adhesive before and after high-temperature treatment exhibit identical peak positions, demonstrating excellent thermal stability (Figure S4). Further, attributed to the evaporation of physically condensed water, differential scanning calorimetry (DSC) and thermogravimetric (TG) analyses reveal a weak exothermic peak and slight mass loss at 98°C, with the material remaining stable at other temperatures for the Al_2O_3 adhesive (Figures S5 and S6).

First, the basic characteristics of the light-emitting layer were investigated, and the PL and PLE spectra demonstrate that the KSF: Mn^{4+}@Cu substrate (K@Cu) can be efficiently excited by 450 nm blue light and exhibits an ultra-narrow emission peak centered at 691 nm with a full width at half maximum (FWHM) of 7.5 nm, which is consistent with the luminous characteristics of KSF: Mn^{4+} phosphor (Figure 2a). Considering the relatively poor thermal quenching of KSF: Mn^{4+}, efficient thermal management is indispensable, with interfacial coupling between the KSF: Mn^{4+} and the Cu substrate markedly enhancing the luminescence intensity at an identical temperature (Figure 2b; Figures S7–S9). The sintering-free fabrication strategy overcomes the limitation that the KSF: Mn^{4+} luminescent layer cannot be formed on high-thermal-conductivity low-cost metal substrates because of the mismatch in thermal expansion coefficients. This approach not only protects KSF: Mn^{4+} particles from thermal degradation during high-temperature processing but also enables the photoluminescence quantum yield (PLQY) of K-TB@Cu to reach a level comparable to that of KSF: Mn^{4+} (Figure S10). Similar luminescence decay behaviors are observed for the KSF: Mn^{4+} powder and the K@Cu (Figure S11).

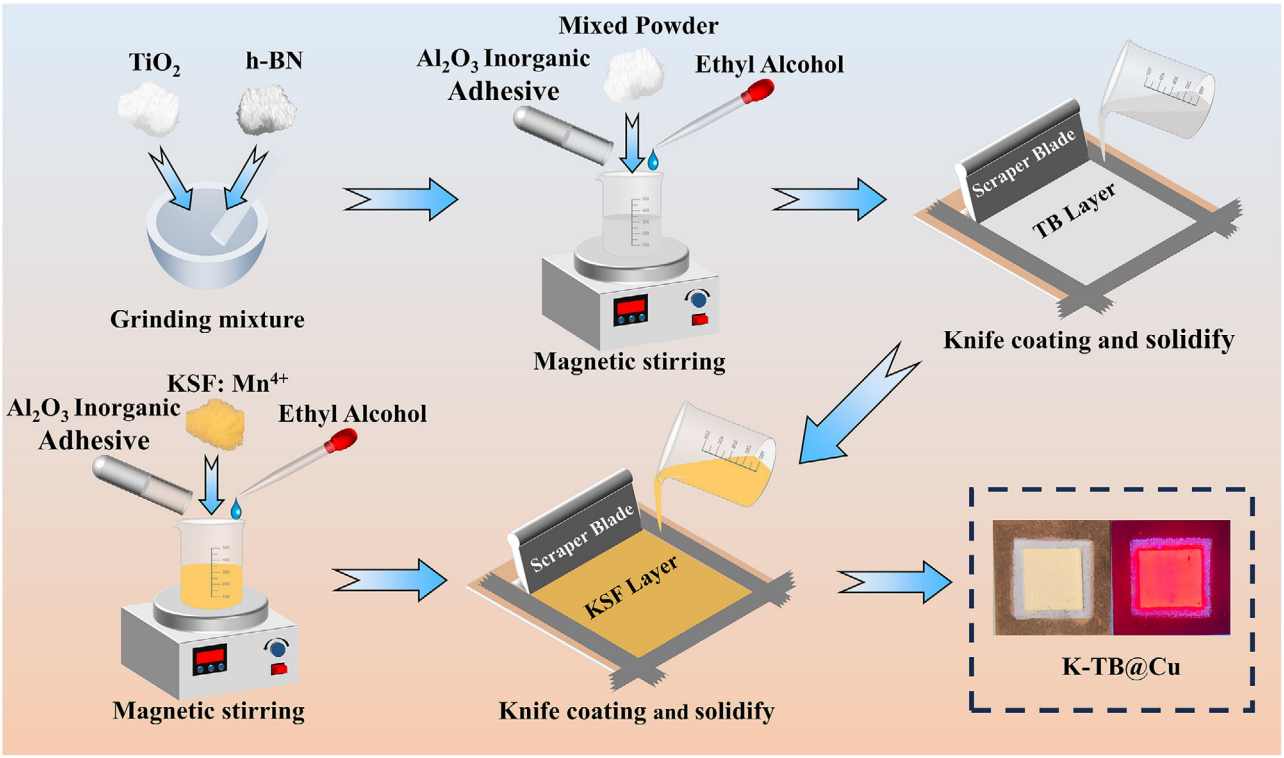

FIGURE 1 | Schematic illustration of the fabrication procedure for K-TB@Cu.

Subsequently, the microstructural characteristics of the proposed composite were investigated. The x-ray diffraction (XRD) patterns of the KSF: Mn^{4+} powder and the K@Cu are consistent with their corresponding standard reference cards, which indicates that no additional impurity phases are generated during the sintering-free preparation process (Figure 2c). Microscopic fluorescence imaging reveals that the K@Cu exhibits highly uniform luminescence and forms a well-defined continuous interface with the underlying Cu substrate (Figure 2d). Further, to overcome the low visible-light reflectivity of the Cu substrate, which restricts the effective luminescence of KSF: Mn^{4+}, a TB transition layer was introduced (Figure S12). The TB layer fulfills two principal functions by effectively suppressing the visible-light absorption of the Cu substrate while simultaneously compensating for the decline in thermal conductivity induced by the incorporation of an additional interfacial transition layer. A comprehensive evaluation of the thermal parameters exhibited that K-TB@Cu exhibited excellent thermal conductivity and heat dissipation capabilities (Table S1). Meanwhile, a detailed XRD analysis was conducted, revealing diffraction patterns consistent with standard reference cards (Figure S13). With the TB layer introduced, the multilayer architecture of the K-TB@Cu (Figure 2f) can be unambiguously resolved by energy-dispersive x-ray spectroscopy (EDS) elemental mapping (Figure 2e), cross-sectional scanning electron microscopy (SEM) (Figure 2g), and fluorescence imaging (Figure 2h).

Upon blue laser irradiation, the luminescence performance of the K-TB@Cu is primarily governed by several key parameters, including the thickness, the relative proportion of TiO_2 and h-BN in the TB layer, and the mass ratio between the Al_2O_3 adhesive and KSF: Mn^{4+} phosphor (Figure 3a–c; Figures S14–S23). The simultaneous temperature monitoring during laser irradiation reveals that increasing the mass ratio of KSF: Mn^{4+} initially helps enhance the red light output power but concurrently induces significant surface temperature rise, which lowers the luminescence saturation threshold and highlights an intrinsic trade-off between luminous performance and thermal management that must be carefully balanced (Figure 3d–f; Note S1). Under the static reflective mode, the optimized red light output power of 399.7 mW is achieved when employing a two-layer structure and a KSF: Mn^{4+} to Al_2O_3 adhesive mass ratio of 5:6 in the K-TB@Cu with a T1B3 (TiO_2:h-BN mass ratio of 1:3) composition in the TB layer. In contrast, when operating under the rotated reflective mode, the K-TB@Cu exhibits significantly superior performance compared to the static mode. Specifically, it delivers a maximum red light output power of 3029 mW (Figure 3g; Figure S24), while maintaining a relatively low surface temperature of ~52.4°C (Figure 3h). Moreover, the composite preserves 98.7% and 96.0% of its initial integrated luminescence intensity after 180 s and 1 h of continuous 11 W blue laser (4.33 W/mm^2) irradiation, respectively (Figure 3i; Figures S25–S29). Table S2 summarizes the luminous flux/red light power, saturation threshold, full width at half maximum (FWHM), and thermal conductivity of red-emitting color converters for laser-driven lighting sources reported in several representative studies [34, 40–42]. The comparative analysis reveals that the developed color converter in this work exhibits distinct advantages for laser-driven display applications.

The thermal stability and millisecond-scale luminescence decay characteristics of KSF: Mn^{4+} are the primary factors governing the thermal saturation and optical saturation, respectively. Figure 3a–h show that the relative influence of optical and

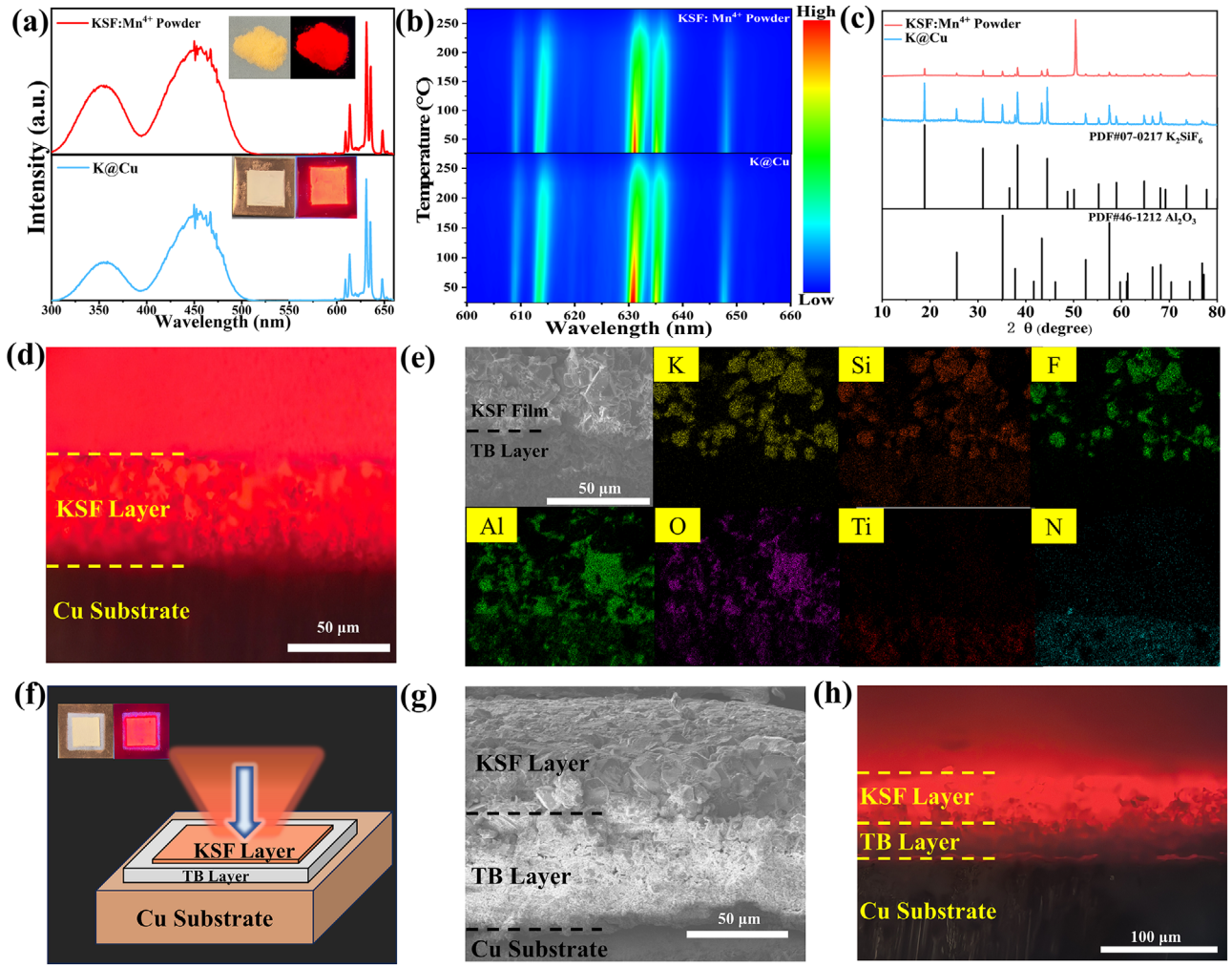

FIGURE 2 | (a) PL and PLE spectra, (b) temperature-dependent PL spectra, and (c) XRD patterns of the KSF: Mn^{4+} phosphor and K@Cu; the insets in (a) present photographs of the samples under natural light and under 450 nm excitation. (d) Cross-sectional microscopic fluorescence image of K@Cu. (e) SEM image and corresponding EDS elemental mapping of the interfacial region between the inorganic KSF: Mn^{4+} luminescent layer and the TB layer. (f) Schematic structural illustration, (g) cross-sectional SEM image, and (h) microscopic fluorescence image of the K-TB@Cu; the insets in (f) display photographs of the K-TB@Cu under natural light and under 450 nm excitation.

thermal saturation on the K-TB@Cu can be quantitatively evaluated (Figure 4a; Note S2) [43]. Variations in the ratio between optical saturation and thermal saturation indicate the relative influence of high-throughput photon excitation versus thermal accumulation at the saturation threshold, with thermal saturation becoming the dominant limiting factor at relatively high KSF: Mn^{4+} concentrations. The incorporation of the TB layer markedly enhances the luminescence performance of K-TB@Cu; specifically, the TiO_2 particles function as an efficient scattering and blocking medium that suppresses the reabsorption of red emission from KSF: Mn^{4+} by the Cu substrate, while the h-BN particles further promote effective thermal dissipation by establishing a continuous heat-conduction network that transfers heat to the high-thermal-conductivity Cu substrate (Figure 4b).

To achieve a laser-driven display, a commercial β-SiAlON: Eu^{2+} phosphor was selected to compensate for the deficient green-light component. With the pattern ratio of KSF: Mn^{4+} and β-SiAlON: Eu^{2+} adjusted, a lighting source suitable for laser-driven display applications was successfully obtained. Spectral analysis indicates that the chromaticity coordinates of the synthesized emission from the K5S3 configuration are located close to the Planckian locus, reflecting a well-balanced contribution of red and green light power (Figure 4c–e). Further, three distinct K5S3 patterns were designed to evaluate the influence of pattern configuration on the luminescence performance, and no discernible differences were observed in either the spectra or the corresponding chromaticity coordinates (Figure 4f–h).

To evaluate the performance of the samples in projection display applications, a prototype laser-driven display system was constructed, consisting of a heat dissipation module and an optical module (Figure 5a). The optical performance of three composites, β-SiAlON: Eu^{2+}/$CaAlSiN_3$:Eu^{2+}-TB@Cu (SC-TB@Cu), β-SiAlON: Eu^{2+}/colloidal quantum dots-TB@Cu (SQ-TB@Cu), and β-SiAlON: Eu^{2+}/K_2SF_6: Mn^{4+}-TB@Cu (SK-TB@Cu), was systematically compared (Figure 5b), with the green emission component in all cases originating exclusively from β-SiAlON:Eu^{2+}. To further elucidate the red-light emission characteristics, the spectra of the three materials were isolated using optical filters

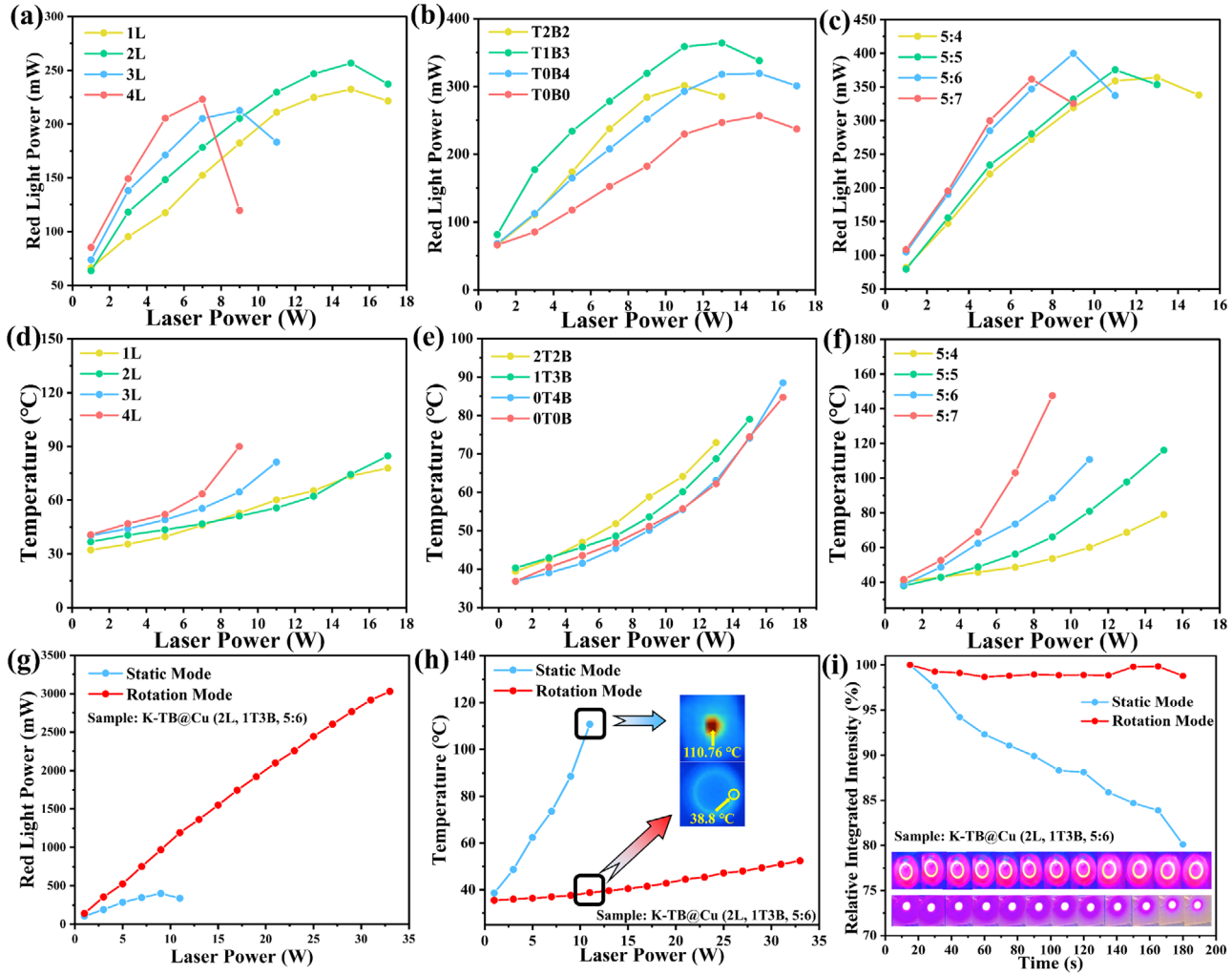

FIGURE 3 | The input laser power dependent red light power variations for K-TB@Cu with varying (a) thickness, (b) the compositional ratio of TiO_2 to h-BN in the TB layer, and (c) the mass ratio of Al_2O_3 adhesive to KSF: Mn^{4+} phosphor powder. (d–f) The corresponding sample surface temperatures. (g) Red-light output power and (h) sample surface temperature of the K-TB@Cu (2L, 1T3B, 5:6) as functions of input laser power under static and rotated modes; the insets in (h) show thermal imaging photographs of the K-TB@Cu irradiated at a laser power of 11 W (4.33 W/mm^2). (i) Time-dependent evolution of the relative integrated emission intensity for the K-TB@Cu (2L, 1T3B, 5:6) operated in s static and rotated modes at a laser power of 11 W (4.33 W/mm^2) over a duration of 180 s; the insets present corresponding photographs.

(Figure 5c). It can be revealed that the SK-TB@Cu exhibits an ultra-narrowband red emission, characterized by a FWHM of only 7.5 nm, which enables highly accurate reproduction of red colors in projected images. For a more intuitive comparison of display performance, the RGB components were extracted from identical positions in the projected images generated by the three composites (Figure 5d; Figure S30). In the display images of red objects, the broadband emission of the SC-TB@Cu results in reduced color purity, as evidenced by pronounced green and blue components in the RGB analysis, while SQ-TB@Cu and SK-TB@Cu both exhibit superior red color performance. However, SQ-TB@Cu suffers from poor operational stability under high-power blue laser excitation, which limits its practical applicability. In addition, a supplementary video further illustrates the dynamic image display performance of the SK-TB@Cu-based device in practical applications (Video S1). Evidently, these results confirm that SK-TB@Cu combines high color purity with strong brightness, highlighting its significant potential for advanced laser-driven display applications.

3 | Conclusions

In summary, by coupling a K_2SiF_6: Mn^{4+} inorganic luminescent layer with a Cu substrate through a sintering-free fabrication strategy, a high-performance narrow-band red-emitting composite was successfully developed. For the TiO_2/h-BN transition layer, the TiO_2 component effectively enhances optical reflectivity and suppresses emission reabsorption by the metallic substrate, while the h-BN component establishes an efficient heat-conduction network, enabling rapid heat dissipation to the Cu substrate. Therefore, the optimized K-TB@Cu composite achieves high optical output and excellent thermal stability, delivering a maximum red output power of 3029 mW under rotated reflective operation while maintaining a low surface temperature and retaining 98.7% of its initial luminescence after prolonged high-power laser irradiation. Further, comparative laser-driven projection display evaluations demonstrate that K-TB@Cu uniquely combines ultra-narrowband red emission, high luminance, and robust laser-driven stability, outperforming con-

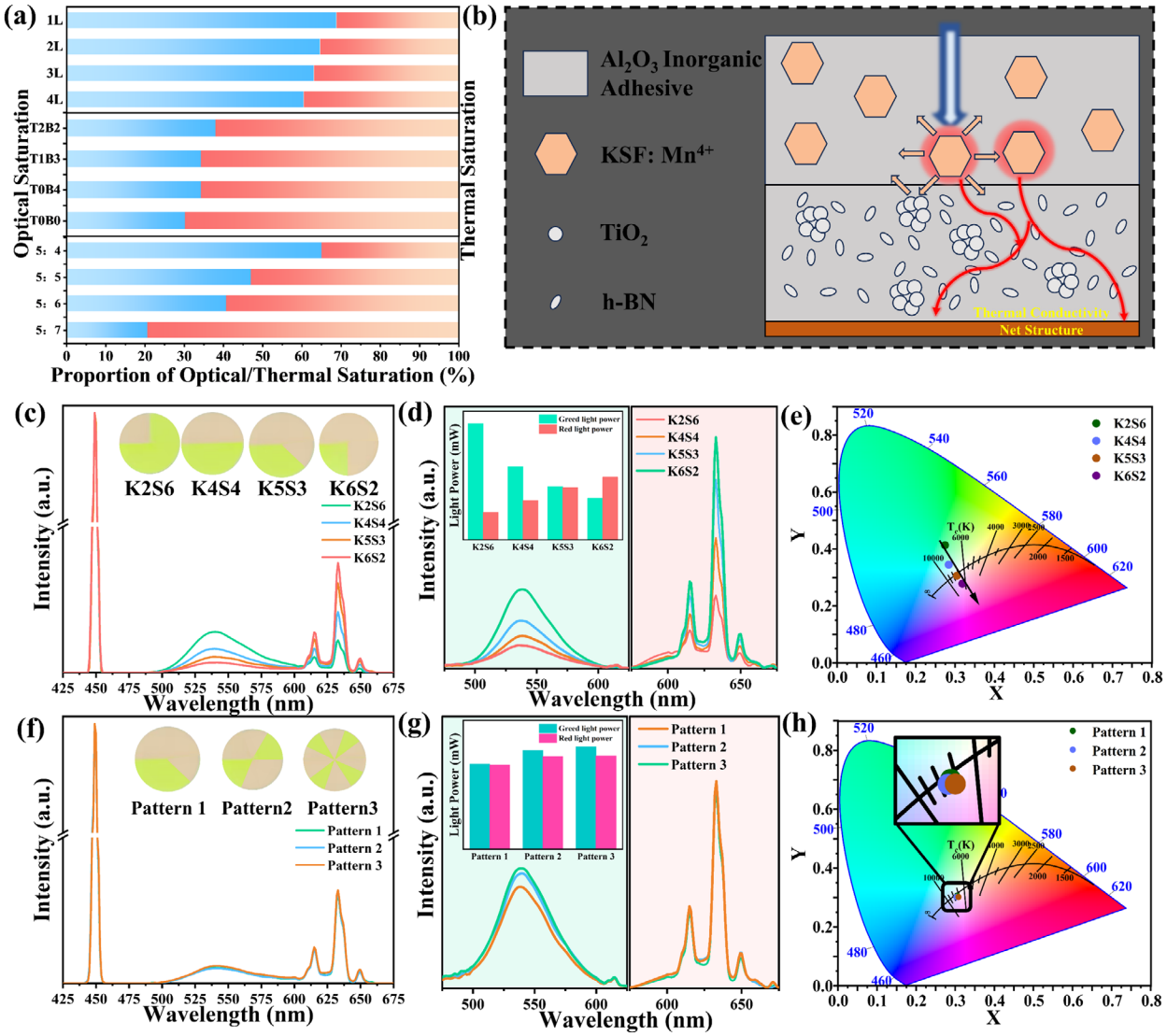

FIGURE 4 | (a) Proportions of the optical and thermal saturation for each sample at the saturation threshold. (b) Schematic illustration of the action mechanism of the TB layer in K-TB@Cu. (c,f) Luminescence spectra, (d,g) the corresponding enlarged spectra in the green and red emission regions, and (e,h) corresponding chromaticity coordinates; the insets of (d) and (g) depict the light power of the green and red emissions, respectively.

ventional nitride- and quantum-dot-based red converters. These results highlight the effectiveness of sintering-free inorganic phosphor-metal integration as a general strategy for laser-driven color converters and position K-TB@Cu as a promising candidate for next-generation high-brightness wide-color-gamut laser-driven display systems.

4 | Experimental Section

4.1 | Fabrication of K-TB@Cu

As shown in Figure 1, mix TiO_2 (Macklin, China), h-BN (Macklin, China), and Al_2O_3 inorganic adhesive (Japan, ThreeBond) and add anhydrous ethanol (Macklin, China) is made into a mixed slurry, the solid-liquid ratio is 1:1; the mass ratios of TiO_2, h-BN and Al_2O_3 adhesive are 2:2:4, 1:3:4 and 0:4:4. The area on the Cu substrate is delineated with adhesive tape to define the coating region, while the coating thickness is precisely regulated by stacking multiple layers of tape. The slurry is spread onto the Cu substrate with a scraper and cured at room temperature for 2 h to form a TB Layer. The KSF: Mn^{4+} (Grirem Advanced Materials Co., Ltd., China) layer was prepared in the same way, with the mass ratios of KSF: Mn^{4+} and Al_2O_3 adhesive being 5:4, 5:5, 5:6, and 5:7.

4.2 | Characterization

The fluorescence imaging of K-TB@Cu was carried out using a combined system of optical microscope (Nikon, Eclipse, Ti2) and fluorescence spectrometer (FLS1000, Edinburgh Instruments). X-ray diffraction (XRD) analysis was conducted using a diffractometer (Rigaku SmartLab), with Cu Kα radiation ($\lambda = 0.154$ nm), a scanning rate of 10°/min, and a scanning 2θ range of 10°–80°. Microstructure analysis and element distribution were conducted using scanning electron microscopy (SEM, COXEM EM-30) combined with EDS (Hitachi SU8220). The photoluminescence char-

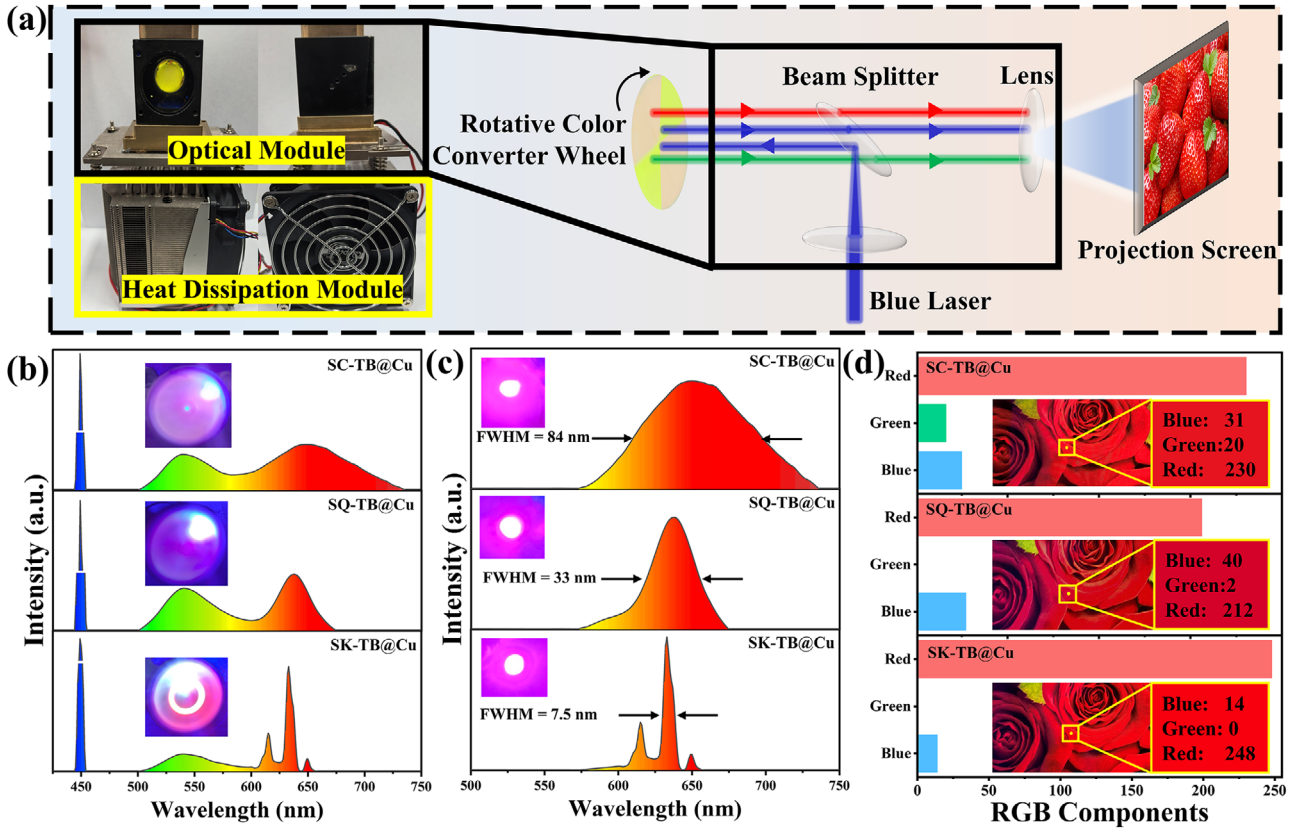

FIGURE 5 | (a) Schematic diagram of the structure for the laser-driven projection display system and the optical path in the reflective excitation mode. (b) Luminicence spectra, (c) red emissions after pass red filter and (d) the RGB value for SC-TB@Cu-based, SQ-TB@Cu-based and SK-TB@Cu-based lighting source; the insets of (b,c) show the corresponding luminescent photographs under blue laser excitation; the insets of (d) are corresponding laser-driven display effects and RGB value taken at the same position in each image.

acteristics (PL, PLE, luminescent decay curves, and PLQY) were tested by a fluorescence spectrometer (FLS1000) equipped with a 450 W xenon lamp. The surface temperature was monitored by the FLUKE infrared thermal imager (TiS75, FLUKE). The optical performance under blue laser excitation was characterized using a custom-built measurement system comprising a 30 cm integrating sphere (Labsphere, Inc.), a 450 nm laser (LSR445CP-FC-40 W, Lasever), a CCD spectrometer (HR4000, Ocean Optics), and a rotary motor (used rotational speed: 3600 rpm). The power of the employed blue laser was meticulously calibrated using a power meter (RK-L0.1, RealPhotonics Co., Ltd.). The evaluated parameters included emission spectra, luminous flux (LF), luminous efficacy (LE), color rendering index (CRI), and CIE color coordinates. The laser beam was focused to a spot with a radius of 0.9 mm, corresponding to an irradiated area of 2.54 mm^2 (Figure S31). The visible light absorption spectrum was obtained by the Techcomp UV2600 spectrophotometer. Thermogravimetry (TG) and differential scanning calorimetry (DSC) measurements were conducted on a Netzsch STA449C thermal analysis system with a heating rate of 10°C min^{-1}.

Author Contributions

S. S. Lin conceived the material design. S. F. Zhuo synthesized the material and wrote the first draft. S. S. Lin and D. Q. Chen helped to analyze the experimental results and finish the final manuscript. H. X. Chen, H. W. Lin, Y. C. Dai, R. An, D. H., and H. X. Qiu helped to measure the spectroscopy. H. X. Chen, X. L. Liu, L. W. Zeng and F. Huang provided constructive suggestions to data analyses. D. Q. Chen supervised the project.

Acknowledgements

This research was supported by the National Natural Science Foundation of China (12304442, 52572155, and 52272141), and the Natural Science Foundation of Fujian Province (2024J02014).

Conflicts of Interest

The authors declare no conflicts of interest.

Data Availability Statement

The data that support the findings of this study are available from the corresponding author upon reasonable request.

References

1. H. Wen, P. Zheng, S. Lin, T. Zhou, and R. Xie, "Sintering-Free Phosphor Films for Laser-Driven Lighting," *Laser & Photonics Reviews* 19 (2025): 2402260, https://doi.org/10.1002/lpor.202402260.

2. J. Sun, Z. Lu, Y. Liu, et al., "A Highly Stable $CsPbBr_3$–SiO_2 Glass Ceramic Film Sintered on a Sapphire Plate for Laser-Driven Projection Displays," *Journal of Materials Chemistry C* 10 (2022): 17109–17118, https://doi.org/10.1039/D2TC04160J.

3. Z. Yu, J. Zhao, Z. Yang, et al., "A Novel PiGF@Diamond Color Converter With a Record Thermal Conductivity for Laser-Driven Projection Display," *Advanced Materials* 36 (2024): 2406147, https://doi.org/10.1002/adma.202406147.

4. Y. Xu, S. Li, P. Zheng, et al., "A Search for Extra-High Brightness Laser-Driven Color Converters by Investigating Thermally-Induced Luminance Saturation," *Journal of Materials Chemistry C* 7 (2019): 11449–11456, https://doi.org/10.1039/C9TC03919H.

5. H. Zhang, H. Li, A. A. Haider, et al., "An Unexpected Role of Lanthanide Substitution in Thermally Responsive Phosphors $NaLnTe_2O_7:Eu^{3+}$ (Ln = Y and Gd)," *Chinese Journal of Structural Chemistry* 44 (2025): 100509.

6. Y. Lin, H. Lin, P. Wang, J. Xu, Y. Cheng, and Y. Wang, "$CaLu_2Mg_2Si_3O_{12}:Ce^{3+}$, Cr^{3+}, Nd^{3+} Phosphor-In-Glass Film for Laser-Driven Ultra-Broadband Near-Infrared Lighting With Watt-Level Output," *Laser & Photonics Reviews* 18 (2024): 2400995.

7. X. Li, R. Zhang, X. Wei, Z. Xu, and X. Qin, "Cold Sintered $Ce^{3+}:Lu_3Al_5O_{12}$-$Mn^{4+}:K_2SiF_6$-$Y^{3+}:CaF_2$ Transparent Ceramic Phosphors for High Color Rendering White LEDs/LDs," *Journal of the European Ceramic Society* 45 (2025): 117315.

8. S. Li, L. Wang, N. Hirosaki, and R. Xie, "Color Conversion Materials for High-Brightness Laser-Driven Solid-State Lighting," *Laser & Photonics Reviews* 12 (2018): 1800173, https://doi.org/10.1002/lpor.201800173.

9. Y. Mou, B. Tian, X. Liu, et al., "High Color Quality Laser-Driven White Lighting Enabled by Reflective Bicolor Phosphor-In-Glass Film Converter," *Journal of Rare Earths* 43 (2025): 1844–1851, https://doi.org/10.1016/j.jre.2024.06.020.

10. J. Zheng, J. Liu, G. Wu, et al., "High-Thermal-Conductivity YAGG:Ce Color Converters on AlN Substrate Enabling High Power and Superior Luminance in Static and Dynamic Reflective Laser Illumination," *Journal of Rare Earths* 43 (2025): 2629–2636, https://doi.org/10.1016/j.jre.2024.12.024.

11. Z. Yang, S. Lin, S. Zheng, et al., "High-Efficiency Red-Emitting Phosphor-in-Glass Films for Laser-Driven Lighting and Display," *Laser & Photonics Reviews* 20 (2025): 02185.

12. D. Zhang, W. Xiao, C. Liu, et al., "Highly Efficient Phosphor-Glass Composites by Pressureless Sintering," *Nature Communications* 11 (2020): 2805.

13. Y. Mou, J. Zhao, Z. Yu, Q. Wang, M. Chen, and Y. Peng, "Highly Reflective Interface Design for Phosphor-In-Glass Converter Enabling Ultrahigh Efficiency Laser-Driven White Lighting," *Journal of the European Ceramic Society* 42 (2022): 7579–7586.

14. Z. Li, Y. Wei, J. Zhao, et al., "Innovative Microstructure Design of Phosphor-in-Glass Film Converter for Efficient and High-Brightness Laser Lighting," *Advanced Optical Materials* 13 (2025): 02398.

15. S. Li, Y. Guo, and R.-J. Xie, "Laser Phosphors for Next-Generation Lighting Applications," *Accounts of Materials Research* 3 (2022): 1299–1308, https://doi.org/10.1021/accountsmr.2c00193.

16. H. Tong, H. Li, W. Liu, and G. Ouyang, "Lead-Free Organic Antimony Halide With Dual-Band Intrinsic White Light Emission for Warm WLED Directly," *Chinese Journal of Structural Chemistry* 44 (2025): 100678.

17. S. Zhu, S. Jin, L. Zhan, et al., "Glass Network Engineering of Yellow-Emitting $Ba_2Sc_2B_4O_{11}:Ce^{3+}$ Glass Ceramics for Full-Spectrum Lighting," *Journal of Advanced Ceramics* 14 (2025): 9221169, https://doi.org/10.26599/JAC.2025.9221169.

18. H. Cheng, Y. Wang, J. Zhao, et al., "Multi-Channel Thermal Conductive Phosphor-In-Glass Film With a Record Laser Power Density Threshold for Laser Lighting," *Chemical Engineering Journal* 521 (2025): 166737, https://doi.org/10.1016/j.cej.2025.166737.

19. T. Pang, S. Lin, F. You, et al., "Synergistic Enhancement of Crystallinity and Transparency in Tb^{3+}-Doped Nano-Glass-Ceramics for High-Resolution X-Ray Imaging," *Journal of Advanced Ceramics* 14 (2025): 9221122.

20. Z. Yang, S. Zheng, G. Xi, et al., "Patterned Phosphor-In-Glass Films With Efficient Thermal Management for High-Power Laser Projection Displays," *Journal of Advanced Ceramics* 12 (2023): 2075–2086, https://doi.org/10.26599/JAC.2023.9220809.

21. J. Park, J. Kim, and H. Kwon, "Phosphor–Aluminum Composite for Energy Recycling With High-Power White Lighting," *Advanced Optical Materials* 5 (2017): 1700347, https://doi.org/10.1002/adom.201700347.

22. P. Wang, H. Lin, G. Chen, et al., "Rapid Sintering of High-Efficiency Phosphor-In-Glass Films for Laser-Driven Light Source," *Nature Communications* 16 (2025): 2807.

23. Y. Sun, Y. Wang, W. Chen, et al., "Rapid Synthesis of Phosphor-Glass Composites in Seconds Based on Particle Self-Stabilization," *Nature Communications* 15 (2024): 1033, https://doi.org/10.1038/s41467-024-45293-0.

24. C. Yan, X. Ding, M. Chen, Y. Liang, S. Yang, and Y. Tang, "Research on Laser Illumination Based on Phosphor in Metal (PiM) by Utilizing the Boron Nitride-Coated Copper Foams," *ACS Applied Materials & Interfaces* 13 (2021): 29996–30007, https://doi.org/10.1021/acsami.1c03746.

25. T. Deng, L. Huang, S. Li, et al., "Thermally Robust Orange-Red-Emitting Color Converters for LASER-Driven Warm White Light With High Overall Optical Properties," *Laser & Photonics Reviews* 16 (2022): 2100722, https://doi.org/10.1002/lpor.202100722.

26. Z. Yu, Y. Mou, Y. Peng, D. Chen, and M. Chen, "Toward High-Brightness Laser Lighting: Progress and Perspectives on Phosphor-In-Glass Films," *Advanced Materials Technologies* 10 (2025): 2402050.

27. Z. Yang, S. Zheng, S. Zhuo, et al., "Toward Laser-Driven Lighting With High Overall Optical Performance: Thermally Robust Composite Phosphor-in-Glass Film," *Laser & Photonics Reviews* 19 (2025): 2401798, https://doi.org/10.1002/lpor.202401798.

28. Y. Kuang, Y. Sun, W. Chen, Y. Wang, and Z. Xia, "Integrating High Efficiency and Thermal Reliability Photoluminescence in Double-Sapphire-Sandwiched Phosphor-in-Glass Film for Laser Projection Displays," *Advanced Functional Materials* 36 (2025): 20133.

29. D. Hu, S. Lin, T. Pang, et al., "Ultra-Narrowband Green-Emitting Transparent Composite Ceramics for Laser-Driven Display," *Advanced Materials* 37 (2025): 2414957, https://doi.org/10.1002/adma.202414957.

30. S. Liao, S. Jin, T. Pang, et al., "Novel Color Converters for High Brightness Laser-Driven Projection Display: Transparent Ceramics–Glass Ceramics Film Composite," *Advanced Functional Materials* 34 (2024): 2307761, https://doi.org/10.1002/adfm.202307761.

31. G. Xi, S. Lin, T. Shen, et al., "Transparent Ceramic@ Sapphire Composites for High-Power Laser-Driven Lighting," *Advanced Science* 12 (2025): 2505232.

32. S. Liao, Z. Yang, J. Lin, et al., "A Hierarchical Structure Perovskite Quantum Dots Film for Laser-Driven Projection Display," *Advanced Functional Materials* 33 (2023): 2210558, https://doi.org/10.1002/adfm.202210558.

33. Y. Kuang, W. Chen, Y. Wang, Y. Sun, J. Jin, and Z. Xia, "Narrow-Band Green/Red-Emitting Glass Composites Enabling Highly Stable Patterned Wheel for Laser Phosphor Display," *Science China Materials* 68 (2025): 1822–1829.

34. W. Chen, Y. Wang, J. Xu, et al., "Red-Emitting Cordierite Ceramic Enabling General Healthy Warm White Laser Lighting," *Laser & Photonics Reviews* 18 (2024): 2300963, https://doi.org/10.1002/lpor.202300963.

35. W. Chen, Y. Wang, G. Liu, Y. Sun, and Z. Xia, "Si/Al Order and Texture Orientation Optimization of Red-Emitting $Mg_2Al_4Si_5O_{18}:Eu^{2+}$ Ceramics for Laser Phosphor Display," *Journal of Materiomics* 10 (2024): 1137–1143.

36. S. Zhuo, S. Lin, T. Pang, et al., "Transparent Ceramic-Quantum Dots Glass Film Composites with High-Efficiency Thermal Management for Laser-Driven Projection Display," *Advanced Functional Materials* 36 (2025): 16371.

37. X. Liu, M. Chen, J. Zhao, H. Zhang, Y. Peng, and Q. Wang, "Unique Composite Architecture of Phosphor-In-Glass Film Coated on Different

Heat-Conducting Substrates for High-Brightness Laser Lighting," *Journal of Advanced Ceramics* 14 (2025): 9221027.

38. X. Wang, J. Qu, H. Zhang, et al., "A Reflective Sapphire@PiGF@Alumina Color Converter Enabling Ultrahigh Luminescence Laser-Driven White Lighting," *Journal of Advanced Ceramics* 14 (2025): 9221124, https://doi.org/10.26599/JAC.2025.9221124.

39. Q. Huang, H. Lin, B. Wang, et al., "Patterned Glass Ceramic Design for High-Brightness High-Color-Quality Laser-Driven Lightings," *Journal of Advanced Ceramics* 11 (2022): 862–873, https://doi.org/10.1007/s40145-022-0578-2.

40. S. Li, D. Tang, Z. Tian, et al., "New Insights into the Microstructure of Translucent $CaAlSiN_3:Eu^{2+}$ Phosphor Ceramics for Solid-State Laser Lighting," *Journal of Materials Chemistry C* 5 (2017): 1042–1051, https://doi.org/10.1039/C6TC04987G.

41. Z. Yang, T. De Boer, P. M. Braun, et al., "Thermally Stable Red-Emitting Oxide Ceramics for Laser Lighting," *Advanced Materials* 35 (2023): 2301837, https://doi.org/10.1002/adma.202301837.

42. Y. Zhou, C. Yu, E. Song, et al., "Three Birds With One Stone: $K_2SiF_6:Mn^{4+}$ Single Crystal Phosphors for High-Power and Laser-Driven Lighting," *Advanced Optical Materials* 8 (2020): 2000976, https://doi.org/10.1002/adom.202000976.

43. P. Zheng, S. Li, T. Takeda, et al., "Unraveling the Luminescence Quenching of Phosphors Under High-Power-Density Excitation," *Acta Materialia* 209 (2021): 116813, https://doi.org/10.1016/j.actamat.2021.116813.

Supporting Information

Additional supporting information can be found online in the Supporting Information section.

Supporting File 1: lpor71160-sup-0001-SuppMat.docx.

Supporting File 2: lpor71160-sup-0002-VideoS1.mp4.